Available online at www.sciencedirect.com
ScienceDirect
Journal of Power Sources 161 (2006) 648–657
JOURNAL OF POWER SOURCES
www.elsevier.com/locate/jpowsour

Diagnostic examination of thermally abused high-power lithium-ion cells

D.P. Abraham [a], E.P. Roth [b,*], R. Kostecki [c], K. McCarthy [c], S. MacLaren [d], D.H. Doughty [b]

[a] *Chemical Engineering Division, Argonne National Laboratory, Argonne, IL 60439, USA*
[b] *Advanced Power Sources R&D Department, Sandia National Laboratories, Albuquerque, NM 87185, USA*
[c] *Environmental Energy Technologies Division, Lawrence Berkeley National Laboratory, Berkeley, CA 94720, USA*
[d] *Center for Microanalysis of Materials, University of Illinois at Urbana-Champaign, Urbana, IL 61801, USA*

Received 11 March 2006; received in revised form 18 April 2006; accepted 19 April 2006
Available online 30 May 2006

Abstract

The inherent thermal instability of lithium-ion cells is a significant impediment to their widespread commercialization for hybrid-electric vehicle applications. Cells containing conventional organic electrolyte-based chemistries are prone to thermal runaway at temperatures around 180 °C. We conducted accelerating rate calorimetry measurements on high-power 18650-type lithium-ion cells in an effort to decipher the sequence of events leading to thermal runaway. In addition, electrode and separator samples harvested from a cell that was heated to 150 °C then air-quenched to room temperature were examined by microscopy, spectroscopy, and diffraction techniques. Self-heating of the cell began at 84 °C. The gases generated in the cell included CO_2 and CO, and smaller quantities of H_2, C_2H_4, CH_4, and C_2H_6. The main changes on cell heating to 150 °C were observed on the anode surface, which was covered by a thick layer of surface deposits that included LiF and inorganic and organo-phosphate compounds. The sources of gas generation and the mechanisms leading to the formation of compounds observed on the electrode surfaces are discussed.

Keywords: Accelerating rate calorimetry; X-ray photoelectron spectroscopy; Raman spectroscopy; Gas analysis; $LiNi_{0.8}Co_{0.15}Al_{0.05}O_2$

1. Introduction

Cells based on Li-ion chemistries offer significant improvements in specific energy and specific power density over standard nickel metal-hydride and lead-acid cells. Li-ion rechargeable cells are now the standard for mobile communication and computing applications. However, these chemistries have not yet penetrated the commercial market for large-scale uses such as in hybrid-electric vehicles. The most significant impediment to the use of these chemistries is the inherent thermal instability of cell components and the flammability of the organic-based electrolytes. The poor abuse tolerance behavior of these cells becomes even more critical for modules based on large numbers of relatively high-capacity cells. The US Department of Energy (DOE) is addressing this problem through the Advanced Technology Development (ATD) effort as part of the FreedomCAR and Vehicle Technologies Program [1]. The ATD program is a cooperative research effort of several US National Laboratories to advance development and characterization of materials in support of battery manufacturers and the automotive industry.

The thermal abuse response of Li-ion cells has been studied at both the component and cell levels using the calorimetric techniques of accelerating rate calorimetry (ARC) and differential rate calorimetry (DSC) [2–6]. These data have shown that the thermal runaway process can be described as occurring in three stages. In Stage 1, low-rate reactions are initiated at the anode around 90 °C (see Fig. 1a and b) followed by a steadily increasing reaction rate. Significant solid electrolyte interphase (SEI) layer breakdown occurs by 120 °C, which leads to electrolyte reduction at the exposed lithiated graphite anode. In Stage 2, reactions are initiated at the cathode around 140–160 °C, depending on the composition of the active (oxide) material. Stage 3 reactions are characterized by high-rate runaway (peak rates >100 °C min^{-1}) and usually occur at or above 180 °C. Stage 3 reactions are primarily the result of oxygen generation from cathode decomposition and subsequent oxidation of the electrolyte [7,8].

In this article, in an effort to decipher the sequence of events leading to thermal runaway, we present ARC measurements conducted on high-power 18650-type lithium-ion cells. The gases generated during these experiments were analyzed by gas

* Corresponding author. Tel.: +1 505 844 3949; fax: +1 505 844 6972.
E-mail address: eproth@sandia.gov (E.P. Roth).

0378-7753/$ – see front matter © 2006 Elsevier B.V. All rights reserved.
doi:10.1016/j.jpowsour.2006.04.088

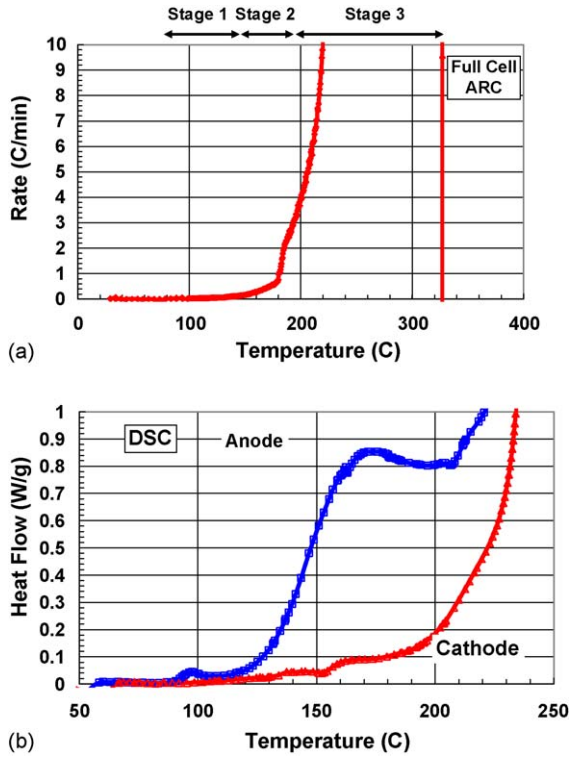

Fig. 1. Calorimetry profiles (at 100% SOC) for an 18650 cell with Mag-10 graphite anode and a $LiNi_{0.8}Co_{0.15}Al_{0.05}O_2$ cathode in 1.2 M EC:EMC (3:7 by wt.) electrolyte. (a) ARC profile showing the three stages of thermal runaway and (b) DSC profile showing the anode/cathode onset reactions.

chromatography/mass spectroscopy (GC/MS). These data are complemented by scanning electron microscopy (SEM), X-ray diffraction (XRD), and X-ray photoelectron spectroscopy (XPS) results obtained on electrodes and separators harvested from a cell that was heated to 150 °C then air-quenched to room temperature (RT) to preserve its thermal history. We discuss the sources of gas generation and possible mechanisms leading to the formation of compounds observed on the electrode surfaces.

2. Experimental

2.1. Cell chemistry and initial conditioning

The ~1 Ah 18650-type cells used in this study (henceforth referred to as Gen2 cells) were manufactured by Quallion LLC (Quallion LLC, P.O. Box 923127, Sylmar, CA 91392-3127, USA). The positive electrode (cathode) contained a 35 μm coating of 84 wt.% $LiNi_{0.8}Co_{0.15}Al_{0.05}O_2$, 4 wt.% SFG-6 graphite, 4 wt.% acetylene black, and 8 wt.% polyvinylidene fluoride (PVDF) binder on a 30-μm-thick Al foil; the active material (oxide) loading density was 8 mg $(cm^2)^{-1}$. The negative electrode (anode) contained a 35 μm coating of 92 wt.% MAG-10 carbon and 8 wt.% PVDF binder on an 18-μm-thick Cu foil; the active material (graphite) loading density was 4.9 mg $(cm^2)^{-1}$. The electrolyte contained 1.2 M $LiPF_6$ in an ethylene carbonate:ethyl methyl carbonate (EC:EMC, 3:7 by wt.) solvent. A 25-μm-thick Celgard 2325 separator provided electronic isolation between the electrodes, while allowing the conduction of lithium ions. Initial characterization tests on the cells included five C/1 cycles between 3.0 and 4.1 V and a C/25 cycle, which confirmed that the cell capacity was ~1 Ah. The cells were then charged to 100% state of charge (SOC) or 4.1 V for subsequent experiments. This voltage is used in the ATD program as the maximum state of charge limit in order to enhance lifetime of the cells during the extended periods of use required for hybrid electric vehicles.

2.2. ARC measurements and cell disassembly

ARC was used to measure the initial thermal response of the cells and to take the cells to a maximum reaction temperature under controlled conditions. The ARC apparatus (Arthur D. Little Model 2000) used a specially designed holder for the 18650 cell that allowed full containment of all generated gases while maintaining good thermal contact with the cell. Monitoring the gas pressure allowed calculation of the evolved gas volume; gas samples were obtained after the run for later GC/MS study. Some of the cells were heated to a maximum temperature of 150 or 160 °C, then cooled rapidly with high flow-rate compressed air. These quenched cells were transferred to an argon glove box and disassembled in the still-charged state. Most of the cathode coating peeled off the Al current collector and adhered to the separator during disassembly, whereas the anode coating remained on the Cu current collector. The cell components were then stored in Ar-bearing hermetic containers until further diagnostic examination.

2.3. Materials examination

Several tools were used to determine the structural, morphological, and compositional changes of the cell components that resulted from heating to elevated temperatures. Most samples were examined "as-harvested," i.e., without prior solvent washing. SEM was conducted on a high-resolution Hitachi S-4700 microscope with a field emission electron source. The samples were briefly exposed to air before insertion into the analysis chamber. X-ray diffraction (XRD) data were collected on a Philips powder diffractometer using Cu-Kα radiation for two-theta values of 20–80°. The samples were examined in a specially designed, hermetically sealed container to avoid any incidental exposure to air.

A LabRam (ISA Groupe Horiba) Raman microscope system was used to analyze the surface structure and composition of the cathode and anode. The excitation source was an internal He–Ne (632 nm) 10 mW laser. The power of the laser beam was adjusted to 0.1 mW. The diameter of the laser beam at the sample was ~1.2 μm. Electrode samples were examined in an airtight optical cell that was assembled in a He-filled glove box prior to the transfer to the Raman microscope. Individual Raman spectra were processed and deconvoluted using the PeakFit 4.0 commercial software package.

XPS spectra were obtained on a Kratos AXIS Ultra spectrometer under ultrahigh vacuum (10^{-9} Torr) conditions. To avoid air exposure, the electrode pieces were mounted on the XPS sample holder in an Ar glove box (<1 ppm H_2O, <5 ppm O_2) and

transported to the analysis chamber under an Ar atmosphere. High-resolution spectra of the C 1s, O 1s, F 1s, P 2p, and Li 1s regions were obtained using monochromatic Al-Kα (1486.6 eV) radiation as the primary excitation source. Because photoelectrons are ejected from a depth of <4 nm, the XPS technique provides information on the concentration and chemical state of elements very near the sample surface. Binding energy scales for the high-resolution spectra were typically calibrated with the graphite peak set to 284.5 eV. Other internal references (hydrocarbon or LiF) were used when graphite was not observed in the spectra.

3. Results

3.1. ARC measurements, gas analysis, and cell disassembly

Fig. 2a shows the ARC temperature and gas volume profile for a cell that was air-quenched to room temperature at 150 °C, while Fig. 2b shows the corresponding temperature and heating rate profiles. Fig. 3 compares the exothermic heating rate data for this quenched cell and a similar cell that was heated to full thermal runaway. The response of the two cells is similar, which indicates that the quenched cell is a good representative of the Gen2 cell chemistry. It is evident from Fig. 2 that self-generated heating in the cell began at 84 °C and continued until the cell was quenched at 150 °C. The cell vented at 124 °C and generated approximately 23 ml of gas (STP) during the entire run.

Fig. 4 shows the normalized composition (by volume) of gases observed in the 150 °C quenched cell; the main gas species

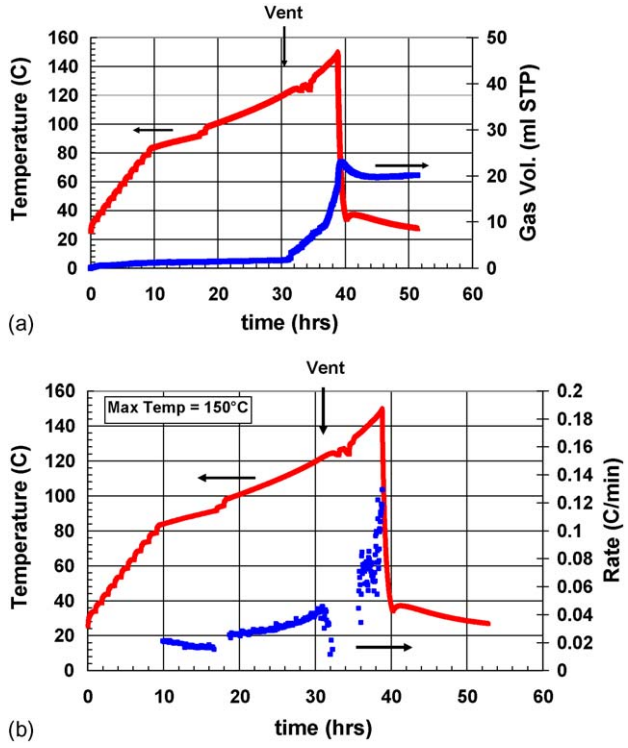

Fig. 2. ARC profiles for an 18650 cell that was heated to 150 °C, then air-quenched to room temperature. (a) Temperature and gas volume generation and (b) Temperature and heating rate.

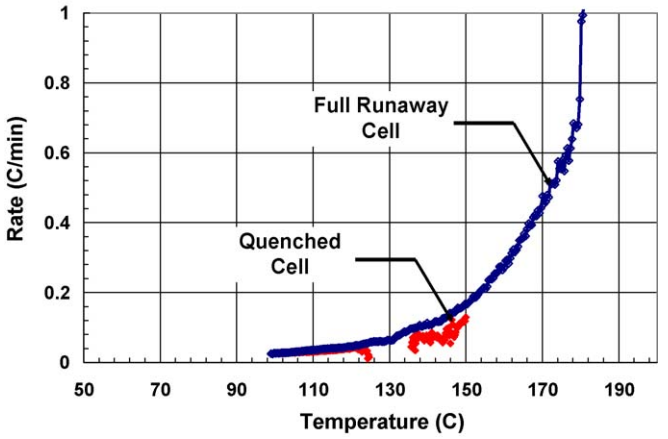

Fig. 3. Comparison of heating rate data on the quenched cell and on another similar cell that was heated to full thermal runaway. Break in data due to cooling from venting cell.

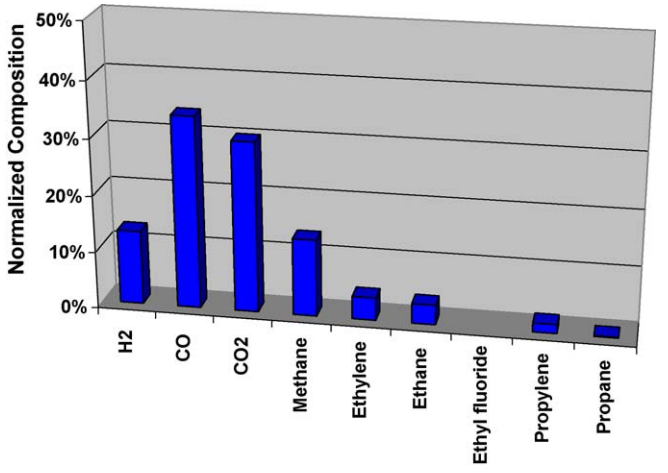

Fig. 4. Composition (by volume) of gases generated in the 150 °C quenched cell.

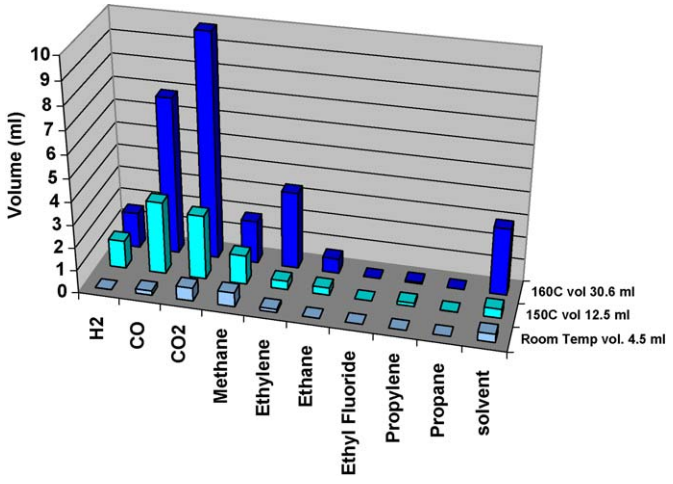

Fig. 5. Gas species in non-vented cells measured at end of ARC runs to 150 and 160 °C. The room temperature data are shown for comparison.

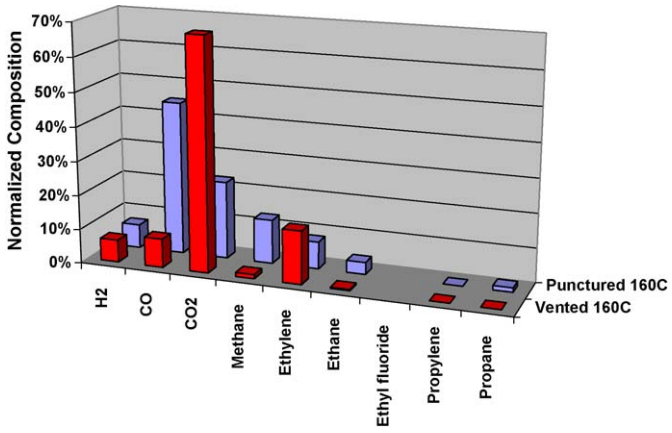

Fig. 6. Normalized gas composition (by volume) of vented and punctured cells heated to 160 °C.

in the cell were CO_2, CO, H_2, C_2H_4, CH_4, and C_2H_6. Fig. 5 shows the gas species in cells that did not vent during a 150 and 160 °C ARC run; data from a RT cell are shown for comparison. These cells were punctured and the extracted gases were introduced directly into a calibrated volume attached to the GC/MS head. The RT cell contained 4.5 ml of gas (initial head space volume) that consisted mostly of CO_2 and CH_4 and some CO. The 150 °C cell contained 12.5 ml of gas primarily resulting from CO, CO_2, and H_2 production in the cell. The 160 °C cell showed a significantly larger gas content primarily resulting from an increase in CO, CO_2, and C_2H_4 contents. The high level of CO measured in the non-vented cells apparently results from anodic reduction of CO_2 at the high cell temperature. This deduction is based on Fig. 6, which shows a significantly higher CO content and a correspondingly lower CO_2 content in the punctured (non-vented) cell relative to that in the vented cell; apparently, the escaped CO_2 in the vented cell can no longer be reduced efficiently at the anode surface.

Cell voltage was often monitored during the ARC run. Most cells showed a drop in cell voltage at the separator shutdown temperature (~135 °C), but the cell voltage rebounded on cooling. For example, the 150 °C quenched cell was measured at 3.84 V just before cell disassembly. The disassembled anode was light bronze in color, which indicated that although some Li diffused out, a substantial amount of intercalated Li was still present in the anode. On storage in inert atmosphere, however, the anode color gradually changed to black.

3.2. Negative electrode examination

3.2.1. SEM and XRD study

The negative electrode contained ~5–10 μm wide Mag-10 graphite, which has a characteristic plate-like morphology and well-defined active edges. A typical micrograph obtained on a formation-only cell (FM) sample (see Fig. 7a) also showed particulates on the graphite surface that includes the electrolyte residue. The SEI layer is not readily apparent in the micrograph because it is very thin (nm size thickness).

A representative micrograph from the 150 °C quenched cell (QC) anode is shown in Fig. 7b. It is apparent that the graphite

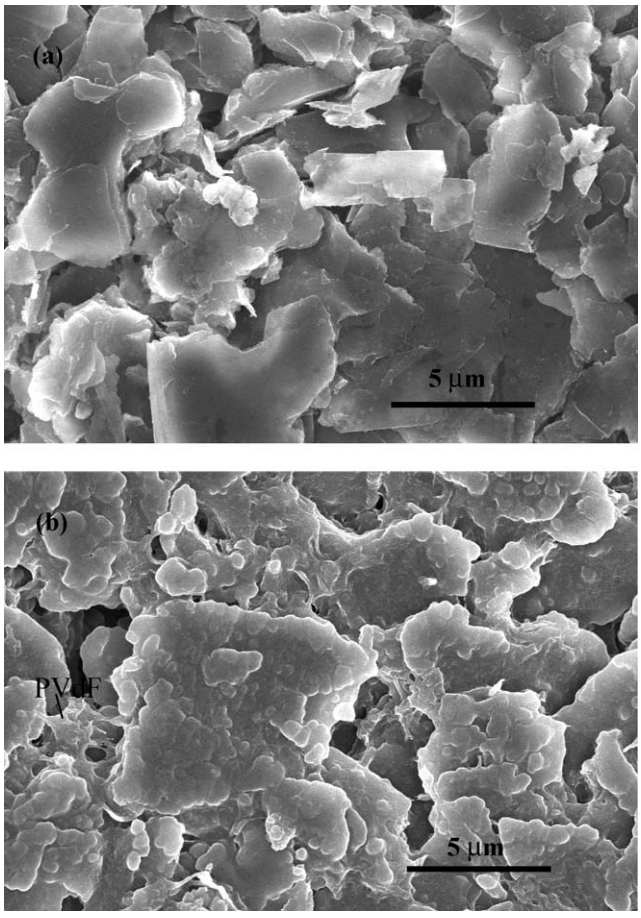

Fig. 7. Typical SEM micrograph from negative electrode sample obtained from (a) the cell that underwent formation cycling only at room temperature and (b) the cell that was heated to 150 °C and quenched.

surfaces are covered by a thick layer of products that results from electrolyte decomposition and/or reaction of Li with the electrolyte. Note the rounding of the graphite particles, which indicates the buildup of reaction products on the edge planes. The PVDF binder that holds graphite particles together shows a distinctly different morphology after heating: the binder apparently melted on heating and then solidified when the cell was quenched to room temperature.

X-ray diffraction data from FM and QC samples are compared in Fig. 8. In both patterns, the most intense peak is Cu(2 0 0) from the copper current collector. The C(0 0 2) and C(0 0 4) peaks from both patterns are very similar, and are typical of Mag-10 graphite. The two-theta, FWHM and XRD counts for the control and QC samples were very similar. There is no indication of bulk graphite amorphization in the QC sample. In addition, peaks that arise from LiC_x compounds formed during graphite-lithiation are not observed in the QC-sample data. Because the QC voltage was 3.84 V just before cell disassembly, the graphite would have contained remnant Li and thus LiC_x peaks should have been observed in the data. The absence of LiC_x peaks suggests that Li continues to diffuse out after cell disassembly and reacted at the graphite surface with electrolyte entrapped in the anode. Had the lithium reacted with electrolyte between the graphene planes, the buildup of reaction products

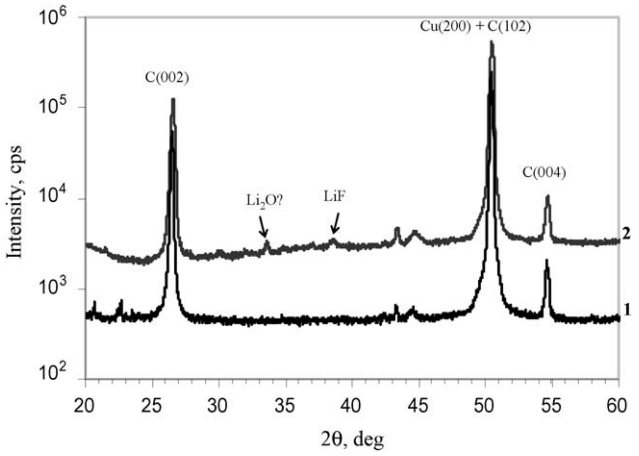

Fig. 8. XRD patterns from negative electrode samples. Sample 1 is from a cell (FM) that was formed and then discharged to 3.1 V. Sample 2 is from a cell (QC) that was charged to 4.1 V, then heated to 150 °C and quenched. The intensity *Y*-axis is shown on a logarithmic scale to highlight the minor peaks in the pattern and the two curves are offset for clarity.

may have altered the graphite d-spacing sufficiently to be evident in the XRD data. Fig. 8 also shows peaks that arise from trace compounds on the graphite surface. For the QC sample, these peaks are consistent with the presence of LiF and Li_2O.

3.2.2. Raman study

Fig. 9a shows Raman microscope spectra recorded at three different locations on the surface of a QC anode sample. Clear spectral evidence of new compounds is observed at all locations, which suggests the presence of a thick and uniform surface layer. The graphite D and G bands at 1335 and 1582 cm^{-1} are completely obscured by signals from the surface layer. The absence of a second-order peak at 2660 cm^{-1} (not shown in figure) also indicates that the surface layer screens the graphite from the laser probe.

The spectra exhibit a group of relatively broad bands at 946, 1133, and 1273 cm^{-1} and a large maximum between 1300 and 1800 cm^{-1} with two sharp bands at 1574 and 1589 cm^{-1}. We assign the broad band centered at 946 cm^{-1} to symmetric vibrations of the orthophosphate $(PO_4)^{3-}$ group, most likely from Li_3PO_4. The intense broad band at 1133 cm^{-1} is attributed to symmetric and asymmetric stretching motions of the two non-bridging oxygen atoms bonded to phosphorous atoms in polyphosphate tetrahedras. The broad maximum centered at 1531 cm^{-1} and a weak band at 1273 cm^{-1} are assigned to symmetric vibrations of C=O and C–O groups in polycarbonates, respectively. The broadness of the Raman bands and the absence of clear-cut peaks indicate that there are a variety of polymer conformations present in the surface layer. It is very likely that steric effects, polymer chains of different length, and copolymerization of phosphate and carbonate segments contribute to the large range of $P–O^-$ and $C–O^-$ bond strengths leading to a variety of polymer stoichiometries and bond lengths and angles. The absence of a distinct peak at 1422 cm^{-1} and its associated shoulder at 1493 cm^{-1} indicates that Li_2CO_3 is not present on the electrode surface.

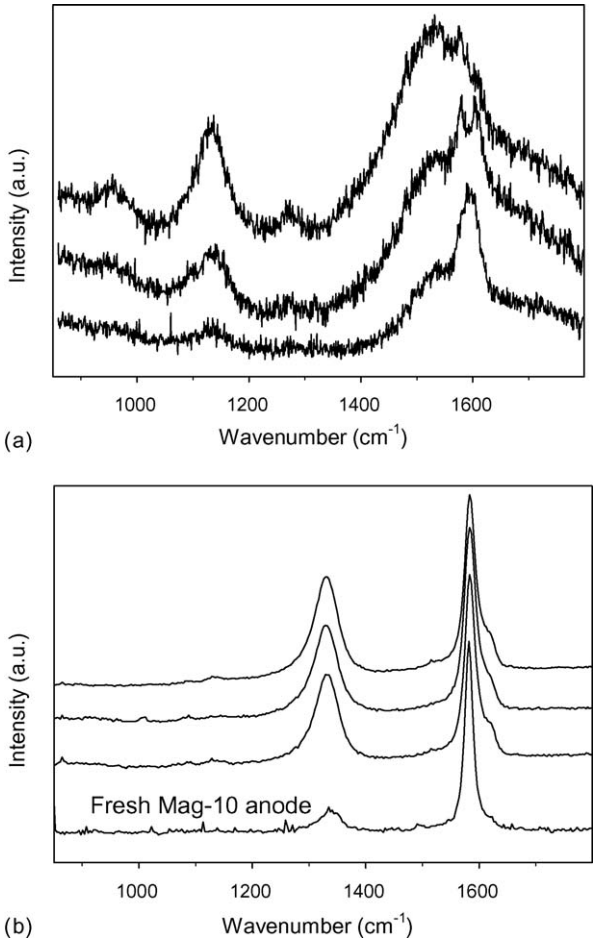

Fig. 9. Raman microscope spectra of the negative electrode from the 150 °C quenched cell (a), and EMC-washed QC sample (b). The three spectra are from three different locations on the electrode surface. A typical spectrum of the fresh Mag-10 negative electrode is also shown.

Fig. 9b shows spectra from three different locations on the 150 °C quenched cell anode sample after it was washed in EMC for 10 min; the typical spectrum from a fresh Mag-10 anode is shown for comparison. The signatures of the surface film are not seen in the washed sample spectra, which indicates that the layer was washed off in EMC. The two graphite bands, G at ~1582 cm^{-1} and D at ~1335 cm^{-1}, are clearly visible in the sample spectra. The G band corresponds to the E_{2g} active mode of graphite. The D band, assigned to the A_{1g} mode, is associated with the breakage of symmetry that occurs at the edges of graphite sheets. The relative D and G peak intensities are noticeably different for the QC sample compared to that of the fresh anode sample. The D band intensity is substantially greater, the G band is significantly broader, and a new sideband at ~1620 cm^{-1} that is typical of disordered carbonaceous materials [9] is observed in the QC sample spectra. The D/G intensity ratio is inversely proportional to the size of graphene domains, and it increases with the extent of carbon disorder. The average D/G intensity ratios are 0.38 and 0.79 for the fresh and QC samples, respectively, which indicate structural damage to the graphite in the thermally abused anode. Note that the results in Fig. 10 apply only to the surface and near-surface regions of

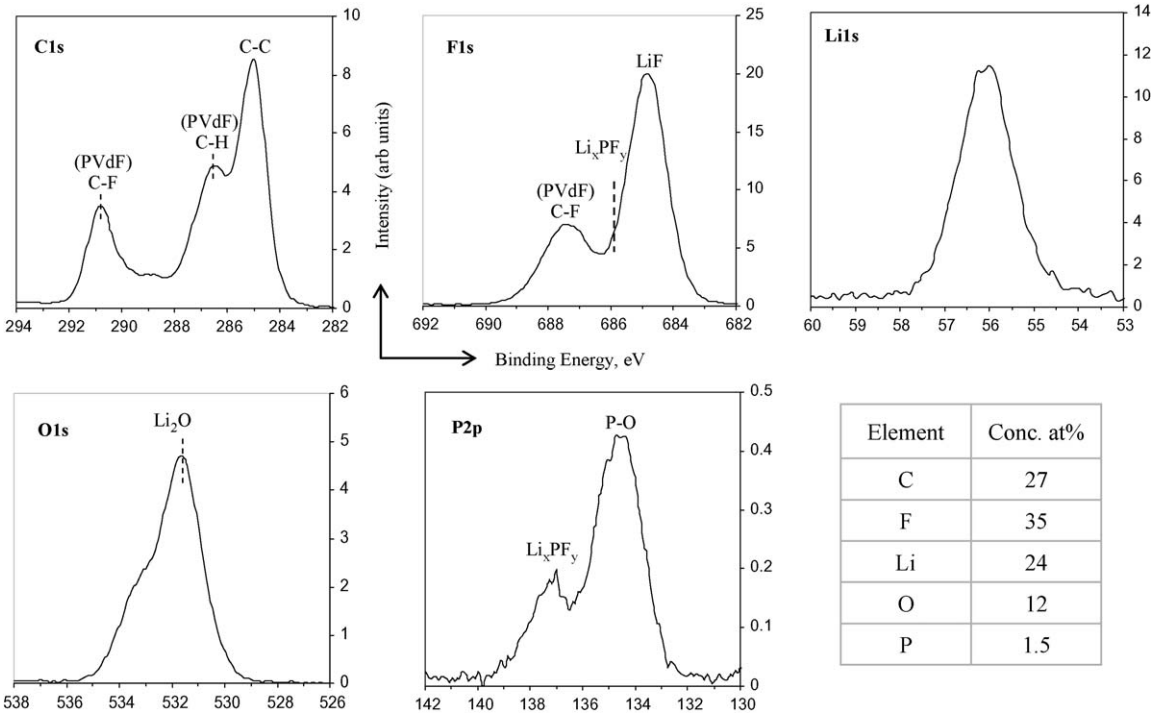

Element	Conc. at%
C	27
F	35
Li	24
O	12
P	1.5

Fig. 10. XPS spectra from negative electrode sample obtained from the 150 °C quenched cell. The binding energy (eV) and normalized intensity (arbitrary units) are shown on the *X*-axis and *Y*-axis, respectively, for all plots. Element concentrations at the electrode surface are also shown in the table.

the anode, i.e., to the depth that the laser probe penetrates into the anode bulk. Similar structural damage to graphite has also been observed in Li-ion cells held at elevated temperatures or examined after prolonged cycling at room temperature [10,11].

3.2.3. XPS study

The C 1s, F 1s, O 1s, and P 2p spectra from the QC anode sample are shown in Fig. 10. Element concentrations measured at the electrode surface are also shown in the figure. The C 1s spectrum contains C–F and C–H peaks arising from the PVDF binder. The C–C peaks do not arise from the graphite particles, which are completely covered by the surface deposits; the peaks arise from other compounds, such as the organophosphates species suggested by the Raman spectroscopy data. Some intensity is also observed in the ~289–290 range, which indicates the presence of carbonates species on the electrode surface. The F 1s spectrum shows a peak at 687.4 eV from the PVDF binder and a very strong LiF peak at 684.8 eV, which is obviously a dominant component of the electrode surface. Contributions from PF_y species present in the electrolyte salt residues are also contained in the F 1s spectrum.

The P 2p spectrum contains a set of $2p_{1/2}$ and $2p_{3/2}$ spin-orbit split peaks for each compound present. The data contain peaks associated with residual Li_xPF_y. The P–O peak intensity in the data may arise from inorganic and organo-fluorophosphates that result from the reaction of the electrolyte with the graphite SEI layer. The O 1s spectrum shows that a significant quantity of oxygen is present on the electrode surface. Because the electrode does not contain this element, the oxygen content must arise from the thermal decomposition of the electrolyte solvent and/or lithium reactions with the electrolyte or electrolyte products. The spectrum also appears to contain a significant quantity of Li_2O, which transforms to Li_2CO_3 on air exposure; the presence of inordinate amounts of Li_2CO_3 on air-exposed samples was confirmed by Fourier transform infrared spectroscopy (FTIR). The Li 1s spectrum contains contributions from several species that include LiF, Li_xPF_y, $Li_xPF_yO_z$, Li_2O, and possibly Li-bearing alkyl fluorophosphate compounds.

3.3. Positive electrode examination

3.3.1. SEM and XRD study

The ~5–10 μm size $LiNi_{0.8}Co_{0.15}Al_{0.05}O_2$ secondary particles in the cathode were made of ~0.2–0.5 μm-size faceted primary particles. The plate-like graphite was ~5–10 μm in width. The acetylene black was <100 nm, irregular shaped with rounded edges, and continuous. The PVDF binder appeared as a thin transparent film covering the oxide and carbon particles. A typical FM sample micrograph showed surface films on the oxide particles that included electrolyte residue and the PVDF binder (see Fig. 11a).

A representative QC sample micrograph is shown in Fig. 11b. There appears to be enhanced separation of the primary particles apparently caused by pressure buildup within the electrode. In addition, the PVDF binder shows a distinct change in its physical characteristics that results from PVDF melting at the elevated temperature and then solidifying on cooling. Examination of the Al current collector showed no indication of enhanced pit formation that could have resulted from the higher test temperature. A change in binder morphology is probably the reason for coating delamination from the Al current collector.

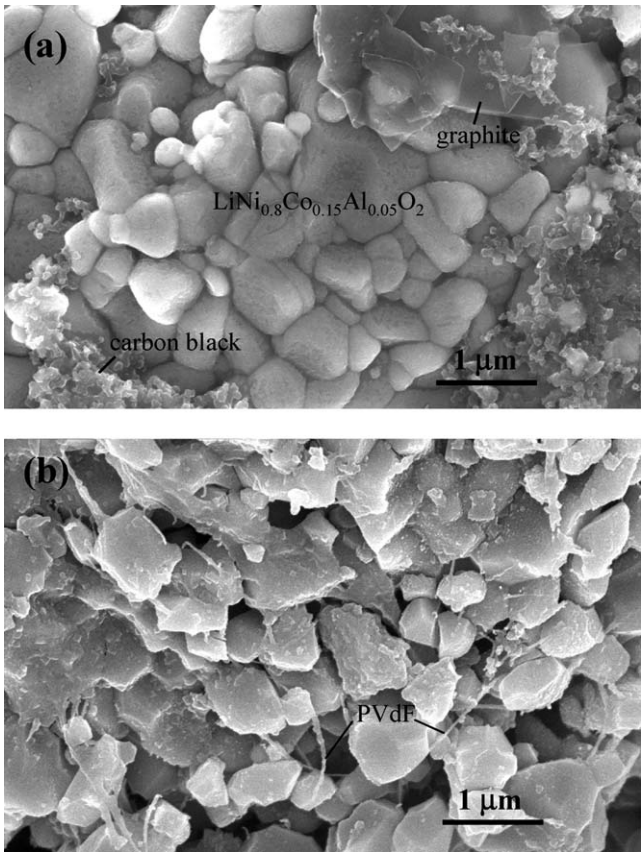

Fig. 11. Typical SEM micrograph from positive electrode sample obtained from (a) the cell that underwent formation cycling only at room temperature and (b) the cell that was heated to 150 °C and quenched.

X-ray diffraction data (Fig. 12) from the QC sample were typical for the electrode. The presence of a sharp C(0 0 2) peak indicated that the graphite was not damaged. The $LiNi_{0.8}Co_{0.15}Al_{0.05}O_2$ peaks were typical for a delithiated oxide; the (0 0 3) to (1 0 4) peak area ratios indicated that the oxide structure was intact. Furthermore, Reitveld refinement of the data showed no indication of lattice disorder and that the structure had retained its oxygen atoms, i.e., there was no oxygen loss from the oxide particles in the 150 °C quenched cell.

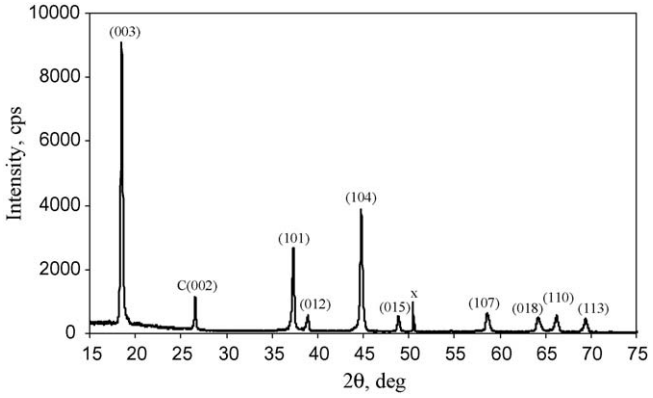

Fig. 12. XRD patterns from the QC positive electrode sample. The C(0 0 2) graphite peak is from the conducting carbons in the electrode. The peak marked *x* is an artifact arising from the sample holder. The remaining peaks are typical of the delithiated oxide.

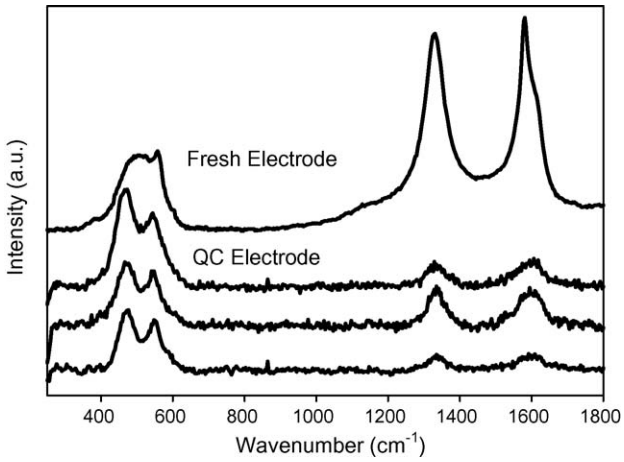

Fig. 13. Raman microscope spectra of a fresh $LiNi_{0.8}Co_{0.15}Al_{0.05}O_2$ cathode and positive electrode sample from the 150 °C quenched cell. The spectra are from three different locations on the electrode surface.

3.3.2. Raman study

Fig. 13 shows Raman microscopy spectra obtained from the QC cathode. The spectra are dominated by two groups of bands. The two peaks at ~470 and ~580 cm^{-1} are characteristic of $Li_{1-x}Ni_{0.8}Co_{0.15}Al_{0.05}O_2$, and the broad peaks at ~1350 and ~1600 cm^{-1} are from the carbon D and G, respectively, that arise from the graphite and carbon black additives. No spectral signature of any surface species was observed in the Raman spectra. When compared to a fresh cathode, the QC cathode showed a much stronger Raman scattering signal from the oxide relative to the carbon additives. These changes in the oxide/carbon concentration ratio may have resulted from electrode delamination and/or mechanical damage induced during cell disassembly.

The oxide bands at 475 and 553 cm^{-1} are associated with the in-plane A_{1g} and E_g vibrations of the NiO_2 lattice. The symmetry of these vibrations in $Li_{1-x}Ni_{0.8}Co_{0.15}Al_{0.05}O_2$ is somewhat distorted by the presence of electronic and coordination structures originating from weak Li–O bonds. The bands tend to broaden, and the 4 7 5/5 5 3 band ratio varies significantly with increasing lithium content in the lattice to form a broad maximum at ~510 cm^{-1} for the fully lithiated $Li_1Ni_{0.8}Co_{0.15}Al_{0.05}O_2$. These band profile changes in the vibrational spectra result from a change in the *a* and *c* parameters of the $Li_{1-x}Ni_{0.8}Co_{0.15}Al_{0.05}O_2$ crystal lattice structure with varying lithium contents. Thus, the level of lithiation can be measured by observing and quantifying changes in the 4 7 5/5 5 3 peak parameters, such as peak intensity ratios [12]. For the QC sample, the 4 7 5/5 5 3 peak ratio varied noticeably as a function of location on the cathode surface, which indicated that the cathode surface SOC varied between individual grains of active material from partially to fully charged. However, it is unclear whether the nonuniform SOC in the cathode existed prior to the cell thermal abuse test or resulted from the elevated temperature testing.

3.3.3. XPS study

The C 1s, F 1s, O 1s, and P 2p spectra from a QC cathode sample are shown in Fig. 14. The intensity (*Y*-axis) has been normalized such that the area under the peaks is proportional to the

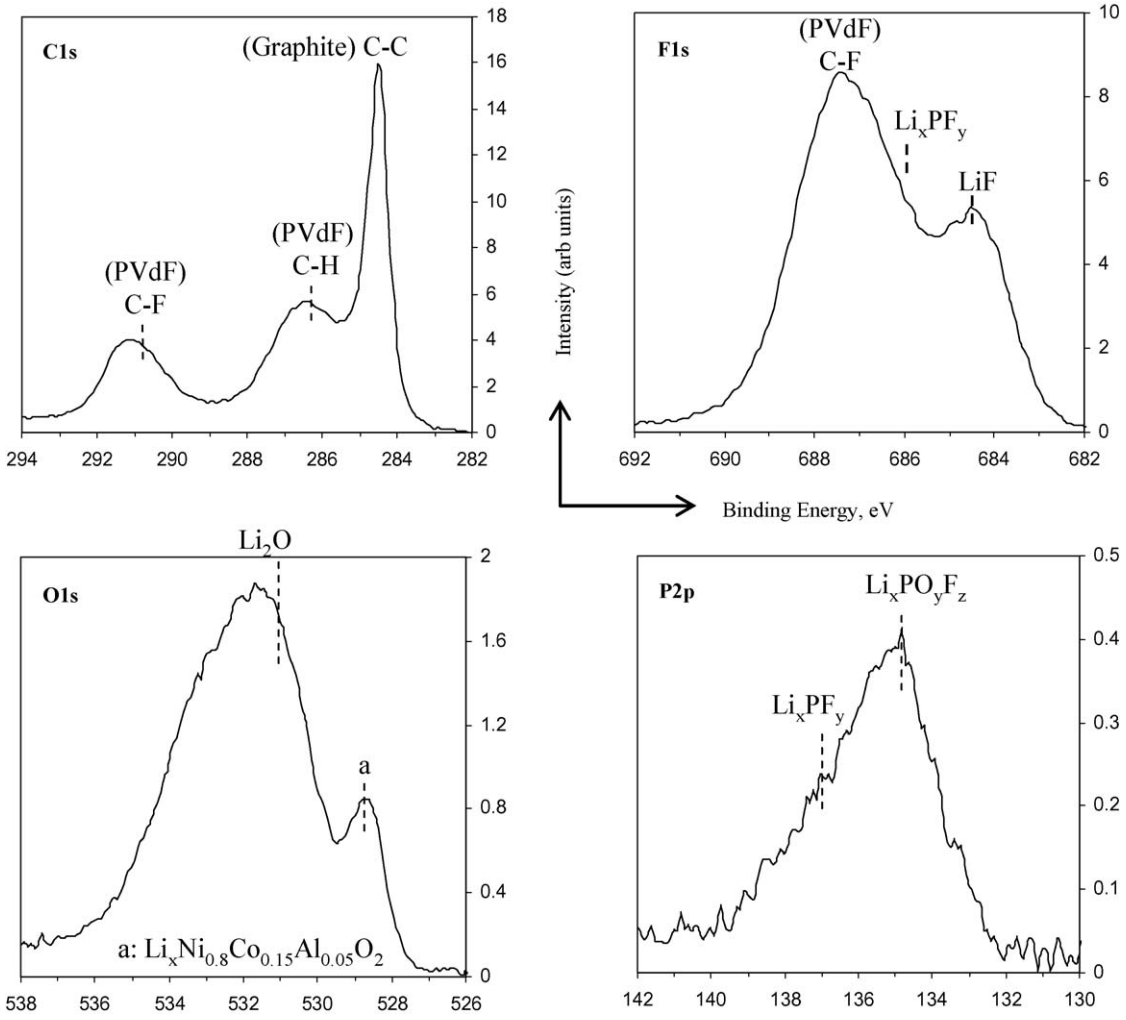

Fig. 14. XPS spectra from positive electrode sample obtained from a cell that was heated to 150 °C and quenched. The binding energy (eV) and normalized intensity (arbitrary units) are shown on the *X*-axis and *Y*-axis, respectively, for all plots.

element concentration measured at the sample surface. The C 1s spectrum contains contributions from graphite, acetylene black, and PVDF ($(–CF_2–CH_2–)_n$). The spectrum is similar to that of FM samples, except for small intensity shifts to higher binding energies in the PVDF regions that suggest some chemical changes in the binder. The F 1s spectrum shows a strong peak at 687.4 eV from the PVDF binder and a distinct peak at 684.5 eV from LiF, which results from $LiPF_6$ decomposition that occurs rapidly above 85 °C.

The P 2p spectrum indicated that the QC samples have less P–F and more P–O content than seen for FM samples, which indicates that phosphate compounds accumulate on the cathode surface during cell heating. The O 1s spectrum shows a distinct peak at 528.6 eV, which arises from the $LiNi_{0.8}Co_{0.15}Al_{0.05}O_2$ particles; this peak is not observed in the FM samples, because the oxide particles are covered by surface films that are produced during formation cycling. The presence of the 528.6 eV peak in the QC sample indicates that the surface films covering the oxide particles are at least partially removed at elevated temperatures. The intensity in the 531 eV to 534 eV regions includes contributions from Li_2O, $Li_xPO_yF_z$, and possibly small amounts of alkyl fluorophosphates species; Li_2CO_3 is excluded because of its absence in the Raman spectroscopy data.

3.4. Separator examination

As mentioned earlier, the cathode coating peeled off the Al current collector and adhered to the separator during disassembly. Therefore, the anode side of the separator was examined by SEM. The effect of elevated temperature testing is shown in Fig. 15. Celgard 2325 is a tri-layer separator with a 25 μm thickness consisting of a polyethylene (PE) layer sandwiched between two polypropylene (PP) layers. Changes in the PP morphology are evident for the QC sample; these fibers appear swollen in Fig. 15. In addition, PE is known to melt at ∼130 °C. At 150 °C, therefore, the PE would have melted, shutting off the separator pores.

4. Discussion

Surface films are present on both the anode and cathode after the initial cell characterization tests. The composition of the

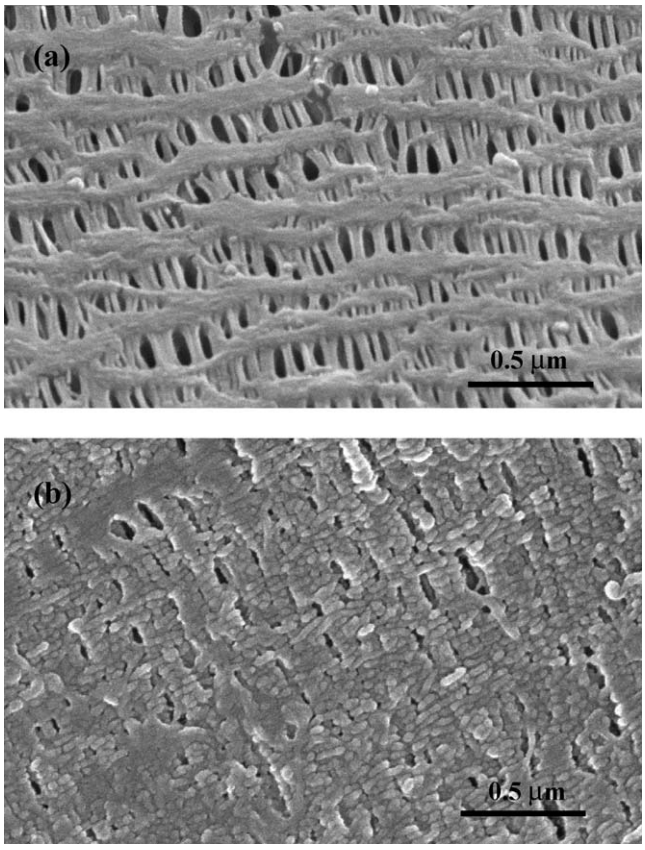

Fig. 15. Typical SEM micrograph of separator sample obtained from (a) the cell that underwent formation cycling only at room temperature and (b) the cell that was heated to 150 °C and quenched.

anode SEI layer is a function of the electrolyte solvent/salt composition and has been examined by several researchers [13–19]. The SEI compounds commonly reported in the literature are organic species such as lithium alkyl carbonates ($ROCO_2Li$) and lithium alkoxides (ROLi), and inorganic products such as Li_2O, LiF, Li_2CO_3, Li_xPF_y, and $Li_xPF_yO_z$. Herstedt et al. [19] reported that EC and EMC reduction products are dominant in the anode SEI layer of 18650 cells that have undergone only initial characterization tests. The cathode surface films mainly contain LiF, Li_xPF_y, and $Li_xPF_yO_z$ compounds; smaller quantities of $ROCO_2Li$ and $ROCO_2R$ species are also present in these surface films [20–22].

In the ARC experiment, self-generated heating in the cell began at 84 °C and continued until the cell was quenched at 150 °C. From our differential scanning calorimetry (DSC) measurements, we know that this heating is initiated at the anode. The organic component of the initial SEI layer is not stable at the higher temperatures and reacts with the electrolyte to form a more inorganic layer [23,24]. Continued heating of the cell accelerates the anode reactions because these inorganic species are brittle and noncompliant during thermal expansion of the electrode and do not form an effective protective layer on the graphite surface. Cracks and delamination in the SEI expose the lithiated anode to the electrolyte, leading to the continued growth/thickening of the layer. The small decrease in voltage during cell heating is consistent with lithium deintercalation from the graphite particles.

Although no significant bulk structure changes were seen in XRD measurements, damage to the graphite surface was observed in the Raman microscopy data. This local degradation/exfoliation may be explained by the high-rate deintercalation of lithium ions from the graphite at elevated temperatures, which leads to structural breakdown and exposure of new graphitic edges and graphitic plane fragments. The released lithium reacts readily with the electrolyte to form a thick layer of products such as polyphosphates and polycarbonates. The freshly exposed active graphite sites are also effective electrocatalysts and react immediately with the electrolyte to form inorganic and organic compounds. These processes result in the rapid accumulation of products at the electrode surface and form a thick barrier between lithiated graphite and the electrolyte.

The gases observed in the cell result mainly from electrolyte decomposition and reduction reactions [25]. These electrolyte decomposition reactions are characterized primarily by solvent decomposition catalyzed by PF_5 arising from the reaction:

$$LiPF_6 = LiF + PF_5$$

An extensive study of the thermal decomposition of $LiPF_6$-based electrolytes has been conducted by Lucht and coworkers using GC/MS and nuclear magnetic spectroscopy [26–28]. They have shown that a mixture of products including CO_2, C_2H_4, fluoroethane (C_2H_5F), diethyl ether [$(C_2H_5)_2O$], flurophosphates [$OPF_2(OCH_2CH_3)$, $OPF_2(OCH_2CH_3)_2$], and flurophosphoric acids [OPF_2OH, $OPF(OH)_2$] are generated during thermal decomposition of a 1 M $LiPF_6$ in diethyl carbonate (DEC) electrolyte. Analogous products are formed during thermal decomposition of 1 M $LiPF_6$ solutions in dimethyl carbonate (DMC) and EMC. In our cells, the EMC-$LiPF_6$ reaction is the main source of gas generation [25]. Some of the resulting species can react with the electrodes, especially the lithiated-carbon, and become part of the products observed on the electrode surfaces. Some of the gases may be from the EC-ring opening induced by PF_5 that produces oligoethercarbonates in the electrolyte, which can transform to oligoethylene oxides by CO_2 evolution [29]. The CO_2 maybe reduced at the anode to form CO, oxalates, and carbonates. The EC-$LiPF_6$ reaction [26] also produces CO_2 and capped oligoethylene oxides [$OPF_2(OCH_2CH_2)_nF$], which can react with the lithiated carbon and be incorporated into the anode SEI.

The positive electrode oxide particles in the 150 °C quenched cell showed no bulk oxygen loss. The stability of the oxide may explain the fewer reaction products observed on the cathode surface relative to that on the anode. In addition, the higher temperature appears to have burned off some of the organic species present on the oxide particles after the initial characterization tests. This increased exposure of the active oxide particles can lead to greater reactivity with the electrolyte. Some of our data have shown that changes to the oxide particles, including oxygen loss from the crystal structure, start around 160 °C [30]. Enhanced oxygen generation at higher cell temperatures and subsequent oxidation of the electrolyte contribute to the

high-rate cathode-electrolyte thermal runaway observed near 180 °C in our DSC measurements.

5. Conclusions

A high-power lithium-ion cell at 4.1 V (100% SOC) was heated to 150 °C and air-quenched to room temperature. Our data show the following: (1) self-generated heating in the cell, initiated at the anode, began at 84 °C and continued until the cell was quenched at 150 °C; (2) the generated gas consisted primarily of CO_2, which was partially reduced to CO at the anode. The gases mainly result from electrolyte decomposition catalyzed by $LiPF_6$ reaction products; (3) the Mag-10 graphite bulk crystal structure was unchanged; however, evidence of graphite damage was observed at the graphite surfaces; (4) the anode graphite was covered by a thick layer of surface deposits, which included LiF and inorganic and organo-phosphate compounds; (5) the $LiNi_{0.8}Co_{0.15}Al_{0.05}O_2$ crystal structure was unchanged, i.e., there was no evidence of oxygen loss from oxide particles in the 150 °C quenched cell; (6) the cathode surface film contained LiF, Li_2O, $Li_xPO_yF_z$, and possibly small amounts of alkyl fluorophosphates species; (7) significant morphological changes resulting from polyethylene melting and polypropylene swelling were observed in the separator; and (8) enhanced oxygen release from the oxide particles is responsible for the cell thermal runaway observed at higher temperatures. Future diagnostic studies will examine components of cells quenched at temperatures just before thermal runaway.

Acknowledgements

This work was supported by the US Department of Energy, Office of FreedomCAR and Vehicle Technologies, as part of the Advanced Technology Development High Power Battery Development Program. Sandia is a multiprogram laboratory operated by Sandia Corporation, a Lockheed Martin Company, for the US Department of Energy's National Nuclear Security Administration under contract DE-AC04-94AL85000. The work at Argonne National Laboratory and Lawrence Berkeley National Laboratory was conducted under Contract Nos. W-31-109-ENG-38 (ANL) and DE-AC03-76SF00098 (LBNL) with the US Department of Energy. The Center for Microanalysis of Materials (CMM) at the University of Illinois at Urbana-Champaign (UIUC) is partially supported by the US Department of Energy under grant DEFG02-91ER45439. We thank Dr. R. Haasch of CMM-UIUC for conducting the XPS measurements. We thank Dr. T. Borek at Sandia for the GC/MS gas analysis and D. Johnson and J. Langendorf for the thermal analysis.

References

[1] E.J. Wall, T.Q. Duong, FY2004 Annual Progress Report, US DOE Freedom CAR and Vehicle Technologies Program, 2005.
[2] E.P. Roth, D.H. Doughty, J. Power Sources 128 (2004) 308–318.
[3] R. Spotnitz, J. Franklin, J. Power Sources 113 (2003) 81–100.
[4] S. Al Hallaj, H. Makeki, J.S. Hong, J.R. Selman, J. Power Sources 83 (1999) 1–8.
[5] J. Shi, C. Lampe-Onnerud, P. Ralbovsky, P. Onnerud, E. Carlsson, B. Barnett, Electrochem. Soc. Proc. 98–16 (1998) 493–499.
[6] H. Maleki, G. Deng, A. Anani, J. Howard, J. Electrochem. Soc. 146 (9) (1999) 3224–3229.
[7] J.R. Dahn, E.W. Fuller, M. Obrovac, U. von Sacken, Solid State Ionics 69 (1994) 265–270.
[8] H. Arai, M. Tsuda, K. Saito, M. Hayashi, Y. Sakurai, J. Electrochem. Soc. 149 (4) (2002) A401–A406.
[9] M. Nakamizo, K. Tamai, Carbon 22 (1984) 197.
[10] R. Kostecki, F. McLarnon, J. Power Sources 550 (2003) 119–121.
[11] E. Markervich, G. Salitra, M.D. Levi, D. Aurbach, J. Power Sources 146 (2005) 146.
[12] J. Lei, F. McLarnon, R. Kostecki, J. Phys. Chem. B 109 (2) (2005) 952–957.
[13] D. Aurbach, Y. Ein-Ely, A. Zaban, J. Electrochem. Soc. 141 (1) (1994) L1–L3.
[14] D. Aurbach, Y. Ein-Eli, B. Markovsky, A. Zaban, S. Luski, Y. Carmeli, H. Yamin, J. Electrochem. Soc. 142 (9) (1995) 2882–2889.
[15] D. Aurbach, J. Power Sources 89 (2000) 206–218.
[16] C.R. Yang, Y.Y. Wang, C.C. Wan, J. Power Sources 72 (1998) 66–70.
[17] A.M. Andersson, M. Herstedt, A.G. Bishop, K. Edstrom, Electrochim. Acta 47 (2002) 1885–1898.
[18] G.V. Zhuang, H. Yang, B. Blizanac, P.N. Ross Jr., Electrochem. Solid-State Lett. 8 (2005) A441.
[19] M. Herstedt, D.P. Abraham, J.B. Kerr, K. Edstrom, Electrochim. Acta 49 (2004) 5097.
[20] A.M. Andersson, D.P. Abraham, R. Haasch, S. MacLaren, J. Liu, K. Amine, J. Electrochem. Soc. 149 (2002) A1358.
[21] D. Aurbach, J. Power Sources 89 (2000) 206–218.
[22] D. Aurbach, J. Power Sources 119–121 (2003) 497–503.
[23] M.N. Richard, J.R. Dahn, J. Electrochem. Soc. 146 (6) (1999) 2068–2077.
[24] M.N. Richard, J.R. Dahn, J. Electrochem. Soc. 146 (6) (1999) 2078–2084.
[25] E.P. Roth, C.C. Crafts, D.H. Doughty, J. McBreen, Thermal Abuse Performance of 18650 Lithium-ion Cells, Sandia National Laboratories Report SAND 2004-0584, 2004.
[26] C.L. Campion, W. Li, B.L. Lucht, J. Electrochem. Soc. 152 (2005) A2327.
[27] B. Ravdel, K.M. Abraham, R. Gitzendanner, J.F. DiCarlo, B.L. Lucht, C.L. Campion, J. Power Sources 805 (2003) 119–121.
[28] C.L. Campion, W. Li, W.B. Euler, B.L. Lucht, B. Ravdel, J.F. DiCarlo, R. Gitzendanner, K.M. Abraham, Electrochem. Solid-State Lett. 7 (2004) A194–A197.
[29] S.E. Sloop, J.B. Kerr, K. Kinoshita, J. Power Sources 119–121 (2003) 330–337.
[30] D.P. Abraham, Argonne National Laboratory, unpublished data.